

# 1       **Global estimates of ambient reactive nitrogen components during** 2                               **2000-2100 based on the multi-stage model**

3       Rui Li<sup>a,b,\*</sup>, Yining Gao<sup>a</sup>, Lijia Zhang<sup>a</sup>, Yubing Shen<sup>a</sup>, Tianzhao Xu<sup>c</sup>, Wenwen Sun<sup>c,\*</sup>, Gehui Wang<sup>a</sup>

4       <sup>a</sup> *Key Laboratory of Geographic Information Science of the Ministry of Education, School of*  
5       *Geographic Sciences, East China Normal University, Shanghai, 200241, PR China*

6       <sup>b</sup> *Institute of Eco-Chongming (IEC), 20 Cuiniao Road, Chenjia Town, Chongming District,*  
7       *Shanghai, 202162, China*

8       <sup>c</sup> *Department of Research, Shanghai University of Medicine & Health Sciences Affiliated Zhoupu*  
9       *Hospital, Shanghai 201318, China*

10      \* **Corresponding author**

11      Prof. Li ([rl@geo.ecnu.edu.cn](mailto:rl@geo.ecnu.edu.cn)) and Prof. Sun ([sunww@sumhs.edu.cn](mailto:sunww@sumhs.edu.cn))

## 12      **Abstract**

13      High contents of reactive nitrogen components aggravate air pollution and could also impact  
14      ecosystem structure and function across the terrestrial-aquatic-marine continuum. However, the  
15      long-term historical trends and future prediction of reactive nitrogen components at the global scale  
16      still remains high uncertainties. In our study, the field observations, satellite products, model output,  
17      and many other covariates were integrated into the multi-stage machine-learning model to capture  
18      the global patterns of reactive nitrogen components during 2000-2019. In order to decrease the  
19      estimate uncertainties in the future scenarios, the constructed reactive nitrogen component dataset  
20      during the historical period was then utilized as the constraint to calibrate the CMIP6 dataset in four  
21      scenarios. The results suggested the cross-validation (CV)  $R^2$  values of four species showed satisfied  
22      performance ( $R^2 > 0.55$ ). The concentrations of estimated reactive nitrogen components in China  
23      experienced persistent increases during 2000-2013, while they suffered from drastic decreases since  
24      2013 except  $\text{NH}_3$ . It might be associated with the impact of clean air policy. However, these  
25      compounds in Europe and the United States remained relatively stable since 2000. In the future  
26      scenarios, SSP3-7.0 (traditional energy scenario) and SSP1-2.6 (carbon neutrality scenario) showed  
27      the highest and lowest reactive nitrogen component concentrations, respectively. Although the  
28      reactive nitrogen concentrations in some heavy-pollution scenarios (SSP3-7.0) also experienced  
29      decreases during 2020-2100, SSP1-2.6 and SSP2-4.5 (middle emission scenario) still kept more

30 rapid decreasing trends. Our results emphasize the need for carbon-neutrality pathway to reduce  
31 global atmospheric N pollution.

## 32 **1. Introduction**

33 Along with the development of global urbanization and industrialization, the anthropogenic  
34 emissions of reactive nitrogen (e.g.,  $\text{NO}_x$ ,  $\text{NH}_3$ ) experienced drastic increases during the past  
35 decades, and caused the higher concentrations of  $\text{NO}_2$ ,  $\text{NH}_3$ , and many secondary components such  
36 as  $\text{NO}_3^-$  ( $\text{NO}_3\text{-N}$ ),  $\text{NH}_4^+$  ( $\text{NH}_4\text{-N}$ ), and  $\text{HNO}_3$  (Chen et al., 2021; Liu et al., 2020b; McDuffie et al.,  
37 2020). The reactive nitrogen released from anthropogenic source could significantly alter the global  
38 nitrogen cycle throughout the Earth system (Altieri et al., 2021; Zhang et al., 2020). Reactive  
39 nitrogen in the atmosphere dominates the chemical formation of tropospheric  $\text{O}_3$  and aggravates the  
40 particle pollution (Geddes and Martin, 2017), with implications for global air quality and climate  
41 change (He et al., 2022; Von Schneidmesser et al., 2015). Moreover, the ambient reactive nitrogen  
42 could be deposited into the land surface and could cause lake eutrophication and soil acidification  
43 (Bouwman et al., 2002; Chen et al., 2018). Therefore, it is highly necessary to understand the spatial  
44 distributions and temporal evolution trends of reactive nitrogen components at the global scale.

45 Despite the global importance, observational constraints on reactive nitrogen in the atmosphere  
46 were still scarce in most parts of the world (Liu et al., 2020b). Furthermore, the majority of  
47 monitoring sites focused on China, Europe, and the United States (Du et al., 2014; Li et al., 2020;  
48 Li et al., 2019a; Li et al., 2016), and these uneven sites only possessed limited spatial  
49 representativeness (Shi et al., 2018), which restricted the accurate assessment of global reactive  
50 nitrogen pollution. Fortunately, the satellite observations gave us a unprecedented chance to capture  
51 the global variations of atmospheric reactive nitrogen. Geddes et al. (2017) used the satellite  
52 products to calibrate the simulated reactive nitrogen oxides ( $\text{NO}_y$ ) and improved the predictive  
53 performance ( $R = 0.83$ ) compared with the chemical transport model (CTM) output alone (Geddes  
54 and Martin, 2017). Afterwards, Liu et al. (2022) also used the similar method to estimate the global  
55 wet deposition of reduced nitrogen ( $\text{NH}_4^+$ ) and the R value achieved 0.80(Liu et al., 2021). Although  
56 the calibration based on satellite products could improve the predictive accuracy compared with  
57 CTM output, the simulated values still largely biased from the ground-level observations. Moreover,  
58 the method cannot accurately fill the gaps of reactive nitrogen concentrations without satellite

59 coverage. In our previous works, we developed a satellite-based ensemble machine-learning model  
60 to predict the wet  $\text{NH}_4^+$  deposition across China and the  $R^2$  value reached 0.76 ( $R = 0.88$ ) (Li et al.,  
61 2020). However, this technique was not expanded to the global scale and the high-accuracy and full-  
62 coverage global ambient reactive nitrogen dataset was still lack.

63 Apart from the historical estimates, the future prediction of reactive nitrogen is also important  
64 because these components in the future scenarios could significantly affect the land carbon cycle  
65 and greenhouse gas emissions, both of which could aggravate the global climate change and affect  
66 the earth system safety (Chen et al., 2015; Zaehle, 2013). To the best of our knowledge, only two  
67 studies focused on global aerosol prediction in the future scenarios. Chen et al. (2023) predicted the  
68 global  $\text{PM}_{2.5}$  levels and associated mortalities in 2100 under different climate scenarios and found  
69 that SSP3-7.0 scenario was linked with the highest  $\text{PM}_{2.5}$  exposure. Li et al., (2022) also simulated  
70 the global  $\text{NO}_3^-$  ( $\text{NO}_3\text{-N}$ ) and  $\text{NH}_4^+$  ( $\text{NH}_4\text{-N}$ ) levels in the future four scenarios and demonstrated  
71 that both of these components showed marked decreases in most cases except SSP5-8.5 scenario.  
72 However, this study predicted the future reactive nitrogen based on historical CTM output alone,  
73 which lacks of observation constraints. The result might increase the uncertainty of assessment.

74 In our study, we developed a multi-stage model to estimate the concentrations of four reactive  
75 nitrogen species ( $\text{NO}_3^-$  ( $\text{NO}_3\text{-N}$ ),  $\text{HNO}_3$ ,  $\text{NH}_3$ , and  $\text{NH}_4^+$  ( $\text{NH}_4\text{-N}$ )) during 2000-2019 because these  
76 species were most important reactive nitrogen components for human health and ecological  
77 ecosystem and also showed abundant ground-level observations. Then, the species over the 2020-  
78 2100 period under the SSP1-2.6, SSP2-4.5, SSP3-7.0, and SSP5-8.5 scenarios were also corrected  
79 based on the historical estimates. Finally, the long-term dataset of reactive nitrogen during 2000-  
80 2100 was constructed. Our results were beneficial to assess the impacts of reactive nitrogen  
81 components on air pollution and climate change in the future.

## 82 **2. Material and methods**

### 83 2.1 Reactive nitrogen observations

84 Most of reactive nitrogen observations focused on East Asia, Europe, and the United States. The  
85 monthly reactive nitrogen components monitoring data during 2010-2015 in China were  
86 downloaded from nationwide nitrogen deposition monitoring network (NNDMN) including 32 sites,  
87 and these sites could be classified into three types mixed with urban, rural, and background sites

88 (Xu et al., 2019) (Table S1). The concentrations of reactive nitrogen components were determined  
89 using the active DENuder for Long-Term Atmospheric sampling system (DELTA). The detailed  
90 sampling and analysis procedures have been described by Xu et al. (2019). The dataset of reactive  
91 nitrogen components in other countries of East Asia during 2000-2019 were download from the  
92 Acid Deposition Monitoring Network in East Asia (EANET), which includes 41 sites. The European  
93 Monitoring and Evaluation Programme (EMEP) provides records of long-term reactive nitrogen  
94 components in 86 sites of most countries across West Europe. Monthly reactive nitrogen  
95 components dataset in 84 locations across the United States could be obtained from the Clean Air  
96 Status and Trends Network (CASTNET) (Figure S1).

## 97 2.2 Data preparation

98 The GEOS-Chem (v13.4.0) model driven by MERRA2 meteorological parameters was applied  
99 to simulate the historical reactive nitrogen components (daily) during 2000-2019 (Feng et al., 2021).  
100 The GEOS-Chem model was composed of detailed ozone-NO<sub>x</sub>-VOC-PM-halogen tropospheric  
101 chemistry. The grid version of the model with a horizontal resolution of 2° × 2.5° was utilized. Wet  
102 deposition contained many processes including sub-grid scavenging in convective updrafts, in-  
103 cloud rainout, and below-cloud washout (Liu et al., 2001). Dry deposition was estimated based on  
104 a resistance-in-series model (Wesely, 2007). The estimates of aerosol optical properties account for  
105 the hygroscopic growth (Drury et al., 2010). Vertical mixing in the boundary layer follows a non-  
106 local scheme implemented by Lin and McElroy (2010), and convection employs the relaxed  
107 Arakawa-Schubert scheme. The anthropogenic emission inventory in 2000-2019 was downloaded  
108 from the website of Community Emissions Data System (CEDS) (Hoesly et al., 2018). CEDS  
109 emission inventory includes eight sectors such as agriculture, energy, industry, residential, shipping,  
110 solvents, transportation, and waste incineration. Then, the daily reactive nitrogen components were  
111 averaged to the monthly scale.

112 The IASI instrument aboard on the polar sun-synchronous MetOp platform traverses the  
113 equator twice each day (9:30 a.m. and 9:30 p.m. local solar time) (Whitburn et al., 2016a). The  
114 measurements in the daytime usually shows the better accuracy than those at night due to the high  
115 sensitivity to ambient NH<sub>3</sub> (Van Damme et al., 2017; Whitburn et al., 2016a; Whitburn et al., 2016b).  
116 In our study, we used the IASI NH<sub>3</sub> columns in morning during 2008-2019 to estimate the NH<sub>3</sub> and

117  $\text{NH}_4^+$  concentrations globally. Besides, the  $\text{NH}_3$  column dataset with a cloud shield higher than 25%  
118 and relative error above 100% were eliminated.

119 The tropospheric vertical column density (VCD) of  $\text{NO}_2$  retrieved from OMI aboard on Aura  
120 satellite crosses the earth once a day (Kim et al., 2016). OMI-derived tropospheric  $\text{NO}_2$  column  
121 densities during 2005-2019 was applied to develop the model. The tropospheric  $\text{NO}_2$  column density  
122 data with cloud radiance fraction  $> 0.5$ , terrain reflectivity  $> 30\%$ , and solar zenith angles  $> 85^\circ$   
123 were screened (Cooper et al., 2022). Additionally, the  $\text{NO}_2$  columns from GOME (1995-2003),  
124 SCIAMACHY (2002-2011) and GOME-2 (2007-) were also collected to simulate the  $\text{NO}_3^-$  ( $\text{NO}_3^-$ -  
125 N) and  $\text{HNO}_3$  levels. The similar overpass time of these three instruments (from about 09:30 to  
126 10:30 LT, local time) facilitates the simultaneous use to capture consistent long-term coverage.  
127 However, the dataset cannot cover the  $\text{NO}_2$  columns since 2017. To overcome the inconsistency of  
128 these satellite products, we applied the linear regression technique to construct the relationship  
129 between OMI- $\text{NO}_2$  columns and GOME/SCIAMACHY  $\text{NO}_2$  columns. The results suggested these  
130 satellite products showed good relationship ( $R^2 > 0.6$ ). At last, the long-term (2000-2019)  $\text{NO}_2$   
131 columns at the global scale were constructed.

132 The monthly meteorological parameters derived from ERA-5 comprise of 2 m dewpoint  
133 temperature ( $D_{2m}$ ), 2 m temperature ( $T_{2m}$ ), surface pressure ( $S_p$ ), and total precipitation ( $T_p$ ), 10 m  
134 U wind component (U10), and 10 m V wind component (V10). The population density data during  
135 2000-2020 around the world were downloaded from  
136 <https://hub.worldpop.org/geodata/listing?id=64>. The elevation data was extracted from ETOPO at a  
137 spatial resolution of 1' (Amante and Eakins, 2009) (<https://rda.ucar.edu/datasets/ds759.4/>). In  
138 addition, the land use types including cropland, forest, grassland, shrubland, tundra, barren land,  
139 and snow/ice were obtained from Liu et al. (2020a). Besides, the CMIP6 dataset in four scenarios  
140 were also applied to predict the reactive nitrogen concentrations during 2020-2100. The dataset  
141 includes 2-m air temperatures, wind speed at 850 and 500 hPa, total cloud cover, precipitation,  
142 relative humidity, and short-wave radiation. The modelled meteorological parameters derived from  
143 16 earth system models were incorporated into the machine-learning model. The detailed models  
144 are summarized in Table S2.

145 2.3 Model development

146 A three-stage model was established to capture the full-coverage reactive nitrogen dataset at  
 147 the global scale (Figure 1). In the first stage, the ground-level reactive nitrogen species, satellite  
 148 products (e.g., OMI-NO<sub>2</sub> and IASI-NH<sub>3</sub> columns), meteorological parameters, land use types,  
 149 population, and simulated reactive nitrogen components derived from GEOS-Chem model were  
 150 collected as the independent variables to estimate the gridded reactive nitrogen species at the  
 151 period/grid with satellite product based on XGBoost algorithm. In the second stage, the  
 152 meteorological parameters, GEOS-Chem output, land use types, and population were applied to fill  
 153 the gaps without satellite retrievals. Then, the simulated results based on these models were fused  
 154 to obtain the full-coverage reactive nitrogen components and the ground-level observations were  
 155 further used to calibrate the full-coverage dataset and the final reactive nitrogen components at the  
 156 global scale were simulated. In the last stage, the reactive nitrogen components and meteorological  
 157 parameters in four scenarios (SSP1-2.6, SSP2-4.5, SSP3-7.0, and SSP5-8.5) during 2020-2100 were  
 158 collected from CMIP6 dataset including 16 earth system models (Table S2). Then, the data in the  
 159 future scenarios were integrated into the ensemble model including XGBoost, LightGBM, and  
 160 convolutional neural networks (CNN) to further calibrate the modeling results based on historical  
 161 dataset (2000-2019) derived from previous two-stage model. The detailed equations of multiple  
 162 machine-learning models are summarized as follows:

163 (1) XGBoost model

$$164 \quad F^{(t)} = \sum_{i=1}^n [l(y_i, \hat{y}_i^{(t-1)}) + \partial_{y_i^{(t-1)}} l(y_i, \hat{y}_i^{(t-1)}) f_t(x_i) + \frac{1}{2} \partial_{y_i^{(t-1)}}^2 l(y_i, \hat{y}_i^{(t-1)}) f_t^2(x_i)] + \Omega(f_t) \quad (1)$$

165 where  $F^{(t)}$  is the cost function at the  $t$ -th period;  $\partial$  is the derivative of the function;  $\partial_{y_i^{(t-1)}}^2$   
 166 represents the second derivative of the function;  $l$  denotes the differentiable convex loss function  
 167 that reveals the difference of the predicted value ( $\hat{y}$ ) of the  $i$ -th instance at the  $t$ -th period and the  
 168 target value ( $y_i$ );  $f_t(x)$  represents the increment;  $\Omega(f_t)$  reflects the regularizer. Maximum tree  
 169 depth and learning rate reached 15 and 0.1, respectively.

170 (2) LightGBM model

$$171 \quad \hat{f} = \arg \min_f E_{y,x} Q(y, f(x)) \quad (2)$$

172 
$$f_T(X) = \sum_{t=1}^T f_t(X) \quad (3)$$

173 where  $Q(y, f(x))$  reflects the a specific loss function;  $\sum_{t=1}^T f_t(X)$  denotes the regression trees.

174 Maximum tree depth, learning rate, and feature fraction reached 25, 0.2, and 0.7, respectively.

175 (3) CNN model

176 The reactive nitrogen species and meteorological parameters in the future scenarios were applied to  
 177 CNN model based on the historical (2000-2019) reactive nitrogen species derived from stage 1-2  
 178 model.

179 
$$x \xrightarrow{f:U-Net} y \quad (4)$$

180 where  $x (x_1, x_2, \dots, x_n)$  represents the reactive nitrogen species and meteorological parameters  
 181 derived from CMIP6 dataset;  $y (y_1, y_2, \dots, y_n)$  denotes the historical (2000-2019) reactive nitrogen  
 182 species.

183 All of the convolution layers showed the same kernel size of  $3 \times 3$  and used rectified linear unit  
 184 (ReLU) as the activation function. Max-pooling layers were employed for adjusting the size of  
 185 images to capture better bottleneck information. After each block, the image size could be halved  
 186 by using the max pooling layer with kernel size of  $2 \times 2$ , but the number of channels will be doubled.  
 187 In our study, the learning rate was set as 0.1 to achieve the best performance.

188 All of the independent variables collected from multiple sources were resampled to  $0.25^\circ$  grids  
 189 using Kriging interpolation. For example, both of the population density and land use types in each  
 190 grid were calculated using spatial clipping toolbox. Later on, all of these variables were combined  
 191 to develop the model. During the development of multi-stage model, it was highly imperative to  
 192 remove some redundant explanatory variables and then determine the optimal variable group. The  
 193 redundant variables means that the overall predictive accuracy could degrade after the removal of  
 194 these variables.

### 195 3. Results and discussion

#### 196 3.1 The modelling performance of historical reactive nitrogen estimates

197 The multi-stage model was applied to capture the spatiotemporal variations of reactive nitrogen  
 198 concentrations during 2000-2100. In our study, we employed XGBoost model to construct the full-

199 coverage reactive nitrogen dataset during 2000-2020. The cross-validation (CV)  $R^2$  values of the  
200 model for  $\text{NO}_3^-$  ( $\text{NO}_3\text{-N}$ ),  $\text{HNO}_3$ ,  $\text{NH}_3$ , and  $\text{NH}_4^+$  ( $\text{NH}_4\text{-N}$ ) estimates reached 0.67, 0.62, 0.58, and  
201 0.60, respectively (Figure 2). RMSE of  $\text{NO}_3^-$  ( $\text{NO}_3\text{-N}$ ),  $\text{HNO}_3$ ,  $\text{NH}_3$ , and  $\text{NH}_4^+$  ( $\text{NH}_4\text{-N}$ ) were 0.55,  
202 0.23, 2.32, and 1.71  $\mu\text{g N m}^{-3}$ , respectively. MAE of  $\text{NO}_3^-$  ( $\text{NO}_3\text{-N}$ ),  $\text{HNO}_3$ ,  $\text{NH}_3$ , and  $\text{NH}_4^+$  ( $\text{NH}_4\text{-N}$ )  
203 N) reached 0.19, 0.13, 1.23, and 0.59  $\mu\text{g N m}^{-3}$ . The CV  $R^2$  values of  $\text{NO}_3^-$  ( $\text{NO}_3\text{-N}$ ),  $\text{HNO}_3$ , and  
204  $\text{NH}_4^+$  ( $\text{NH}_4\text{-N}$ ) estimates were significantly higher than Jia et al. (2016) (0.22, 0.41, and 0.49), while  
205 the CV  $R^2$  value of  $\text{NO}_3^-$  estimate in our study was comparable to Geddes et al. (2017) (0.68)  
206 (Geddes and Martin, 2017). The CV  $R^2$  value of  $\text{NH}_3$  estimates were also close to the results  
207 obtained by Liu et al. (2019) (0.45-0.71) (Liu et al., 2019). Overall, the predictive performances  
208 historical reactive nitrogen was satisfied. Although the CV  $R^2$  values in our study were not  
209 significantly higher than those in some previous studies, our study developed the full-coverage (gap-  
210 free) ambient reactive nitrogen dataset, which was superior to some previous studies. Based on the  
211 constructed full-coverage reactive nitrogen dataset, we also developed the ensemble model to  
212 calibrate the CMIP6 dataset in the future scenarios. The CV  $R^2$  values of the model for  $\text{NO}_3^-$  ( $\text{NO}_3\text{-N}$ -  
213 N),  $\text{HNO}_3$ ,  $\text{NH}_3$ , and  $\text{NH}_4^+$  ( $\text{NH}_4\text{-N}$ ) estimates in the future scenarios reached 0.62, 0.67, 0.56, and  
214 0.60, respectively (Figure S2). RMSE of  $\text{NO}_3^-$  ( $\text{NO}_3\text{-N}$ ),  $\text{HNO}_3$ ,  $\text{NH}_3$ , and  $\text{NH}_4^+$  ( $\text{NH}_4\text{-N}$ ) were 0.58,  
215 0.26, 2.12, and 1.91  $\mu\text{g N m}^{-3}$ , respectively. MAE of  $\text{NO}_3^-$  ( $\text{NO}_3\text{-N}$ ),  $\text{HNO}_3$ ,  $\text{NH}_3$ , and  $\text{NH}_4^+$  ( $\text{NH}_4\text{-N}$ )  
216 N) reached 0.22, 0.22, 1.04, and 0.65  $\mu\text{g N m}^{-3}$ . Overall, the ensemble model for these species in the  
217 future scenarios still showed satisfied performance, and thus the result could be treated to be robust.

### 218 3.2 The spatial patterns of nitrogen reactive components

219 The global annual mean concentrations of  $\text{NO}_3^-$ ,  $\text{HNO}_3$ ,  $\text{NH}_3$ , and  $\text{NH}_4^+$  during 2000-2019  
220 ranged from 0.03 to 9.08, 0.03 to 1.73, 0.21 to 13.9, and 0.08 to 17.1  $\mu\text{g N m}^{-3}$  with the mean values  
221 of  $0.43 \pm 0.24$  (standard deviation over grids),  $0.28 \pm 0.13$ ,  $1.79 \pm 0.85$ , and  $0.65 \pm 0.36$   $\mu\text{g N m}^{-3}$   
222 (Figure S3), respectively. East Asia especially China, West Europe, and the United States obtained  
223 widespread attention due to the developed economy and dense anthropogenic activity.

224 In China, the overall mean ambient  $\text{NO}_3^-$  ( $\text{NO}_3\text{-N}$ ),  $\text{HNO}_3$ ,  $\text{NH}_3$ , and  $\text{NH}_4^+$  ( $\text{NH}_4\text{-N}$ )  
225 concentrations reached  $1.05 \pm 0.62$ ,  $0.35 \pm 0.19$ ,  $4.05 \pm 1.84$ , and  $2.38 \pm 1.26$   $\mu\text{g N m}^{-3}$ , ranging  
226 from 0.07-9.08, 0.06-1.73, 0.84-11.6, and 0.18-13.1  $\mu\text{g N m}^{-3}$ . At the regional scale, the annual mean  
227  $\text{NO}_3^-$ ,  $\text{HNO}_3$ ,  $\text{NH}_3$ , and  $\text{NH}_4^+$  concentrations followed the order of North China Plain (NCP) (4.38,



228 1.12, 7.22, and 7.69  $\mu\text{g N m}^{-3}$ ) > Sichuan Basin ( $2.40 \pm 1.01$ ,  $0.52 \pm 0.28$ ,  $4.92 \pm 1.71$ , and  $6.02 \pm$   
229  $1.82 \mu\text{g N m}^{-3}$ ) (Figure 3). NCP displayed the higher  $\text{NO}_3^-$  and  $\text{HNO}_3$  concentrations owing to dense  
230 human activities and strong industry foundation (Qi et al., 2023; Wen et al., 2018), which could emit  
231 a large amount of  $\text{NO}_x$  to the atmosphere. In both of Yangtze River Delta (YRD) and Pearl River  
232 Delta (PRD), the combustion of fossil fuels and traffic emissions might be the major source of  $\text{NO}_x$   
233 emission, which aggravated nitrate events via gas-particle conversion processes (Huang et al., 2017;  
234 Li et al., 2017). For Sichuan Basin, the poor topographical or meteorological conditions were major  
235 factors responsible for the severe nitrate pollution (Zhang et al., 2019). It was not surprising that  
236 high ambient  $\text{NH}_3$  concentrations focused on NCP and Sichuan Basin because many croplands (dry  
237 land) are distributed on these regions (Karra et al., 2021; Potapov et al., 2022), which was the major  
238 source of  $\text{NH}_3$  emissions with frequent N fertilizer applications (Ma et al., 2022). Besides, N manure  
239 was another major source of  $\text{NH}_3$  emissions in China, and the percentage of N manure to  $\text{NH}_3$   
240 emissions exceeds 50% (Kang et al., 2016). The spatial pattern of  $\text{NH}_4^+$  level was in good agreement  
241 with the  $\text{NH}_3$  concentration because  $\text{NH}_4^+$  was often generated from the reaction of  $\text{NH}_3$  with  $\text{SO}_2$   
242 and  $\text{NO}_2$  (Ehrnsperger and Klemm, 2021). Apart from China, many other countries such as South  
243 Korea and Japan also showed the higher ambient reactive nitrogen concentrations. As shown in  
244 Figure 3, the higher reactive N concentrations occurred on the western coasts of South Korea than  
245 on the eastern coasts. The higher reactive N concentrations in Japan mainly focused on the urban  
246 areas around Tokyo, which might be linked with the dense anthropogenic emission in this region  
247 (Li et al., 2024). In Southeast Asia, Indonesia ( $\text{NO}_3^-$  ( $\text{NO}_3\text{-N}$ ),  $\text{HNO}_3$ ,  $\text{NH}_3$ , and  $\text{NH}_4^+$  ( $\text{NH}_4\text{-N}$ ): 0.18,  
248 0.47, 5.72, and 0.44  $\mu\text{g N m}^{-3}$ ) suffered from the most serious reactive N pollution compared with  
249 other surrounding countries.

250 In Europe, the ambient  $\text{NO}_3^-$  ( $\text{NO}_3\text{-N}$ ),  $\text{HNO}_3$ ,  $\text{NH}_3$ , and  $\text{NH}_4^+$  ( $\text{NH}_4\text{-N}$ ) concentrations ranged  
251 from 0.13 to 2.84, 0.06 to 0.92, 0.35 to 7.81, and 0.22 to 3.77  $\mu\text{g N m}^{-3}$ , respectively. The annual  
252 mean  $\text{NO}_3^-$  ( $\text{NO}_3\text{-N}$ ),  $\text{HNO}_3$ ,  $\text{NH}_3$ , and  $\text{NH}_4^+$  ( $\text{NH}_4\text{-N}$ ) levels reached  $0.57 \pm 0.28$ ,  $0.25 \pm 0.11$ ,  $1.58$   
253  $\pm 0.68$ , and  $0.89 \pm 0.42 \mu\text{g N m}^{-3}$ , respectively (Figure 4). High concentrations of reactive nitrogen  
254 components focused on the northern part of Italy, central and southern part of Germany, North  
255 France, Poland, and the western part of Russia, which was in good agreement with the spatial pattern  
256 of  $\text{NO}_x$  and  $\text{NH}_3$  emissions (Luo et al., 2022; Qu et al., 2020). Emissions Database for Global

257 Atmospheric Research (EDGAR) suggested that N fertilization and N manure accounted for 43%  
258 and 53% of total NH<sub>3</sub> emissions in western Europe (Liu et al., 2019), respectively. Furthermore, Liu  
259 et al. (2019) confirmed that a good relationship between ambient NH<sub>3</sub> level and N fertilization plus  
260 N manure ( $r = 0.62$ ) was observed in Europe. Cooper et al. (2017) employed the inversion model to  
261 estimate NO<sub>x</sub> emission in Europe and also found that high NO<sub>x</sub> emission was also mainly distributed  
262 on North France, Germany, the northern part of Italy, and Russia, which partly explained the higher  
263 concentrations of reactive nitrogen components in these regions.

264 In the United States, the ambient NO<sub>3</sub><sup>-</sup> (NO<sub>3</sub>-N), HNO<sub>3</sub>, NH<sub>3</sub>, and NH<sub>4</sub><sup>+</sup> (NH<sub>4</sub>-N)  
265 concentrations reached  $0.28 \pm 0.12$ ,  $0.19 \pm 0.08$ ,  $2.12 \pm 0.66$ , and  $0.49 \pm 0.25$   $\mu\text{g N m}^{-3}$ , with the  
266 range of 0.03-2.35, 0.03-1.31, 0.26-9.96, and 0.10-6.09  $\mu\text{g N m}^{-3}$  (Figure 5), respectively. The  
267 hotspots of NO<sub>3</sub><sup>-</sup> (NO<sub>3</sub>-N), HNO<sub>3</sub>, and NH<sub>4</sub><sup>+</sup> (NH<sub>4</sub>-N) levels focused on the eastern part of the United  
268 States, while the higher NH<sub>3</sub> concentration focused on Central Great Plains and some regions in  
269 California such as San Joaquin Valley ( $6.15$   $\mu\text{g N m}^{-3}$ ). Both of bottom-up and top-down NO<sub>x</sub> and  
270 NH<sub>3</sub> emissions suggested that the spatial distributions of reactive nitrogen components were  
271 strongly dependent on the precursor emissions (McDuffie et al., 2020; Qu et al., 2020).

272 Besides, some other regions such as India (1.4, 0.5, 6.6, and 4.4  $\mu\text{g N m}^{-3}$ ) especially the  
273 northern part of India (3.1, 0.8, 12.6, and 8.4  $\mu\text{g N m}^{-3}$ ) also experienced severe reactive N pollution  
274 in the atmosphere. Meanwhile, some countries in South America such Brazil and Argentina and in  
275 Africa such as West Africa Coast (Nigeria, Ivory Coast, Ghana, Togo, and Benin) (HNO<sub>3</sub> and NH<sub>3</sub>:  
276 0.3 and 5.0  $\mu\text{g N m}^{-3}$ ) and Democratic Congo (0.4 and 1.6  $\mu\text{g N m}^{-3}$ ) also suffered from serious  
277 HNO<sub>3</sub> (Brazil and Argentina: 0.3 and 0.2  $\mu\text{g N m}^{-3}$ ) and NH<sub>3</sub> (3.6 and 2.8  $\mu\text{g N m}^{-3}$ ) pollution. The  
278 higher ambient NH<sub>3</sub> concentration focused on the northern part of India might be contributed by  
279 two major reasons. First of all, the intensive agricultural activities and high air temperature might  
280 be responsible for the higher NH<sub>3</sub> level (Cui, 2023; Wang et al., 2020). Moreover, the relatively low  
281 sulfur dioxide (SO<sub>2</sub>) and nitrogen oxides (NO<sub>x</sub>) emissions coupled with high air temperature  
282 restricted the gas-to-particle conversion of NH<sub>3</sub> (Wang et al., 2020). The severe HNO<sub>3</sub> and NH<sub>3</sub>  
283 pollution in Brazil, Argentina, and West Africa Coast might be also linked with the dense agricultural  
284 activities (Huneus et al., 2017).

285 3.3 The seasonal variations of reactive nitrogen components

286 The ambient  $\text{NO}_3^-$  ( $\text{NO}_3\text{-N}$ ),  $\text{HNO}_3$ ,  $\text{NH}_3$ , and  $\text{NH}_4^+$  ( $\text{NH}_4\text{-N}$ ) concentrations exhibited  
287 significant seasonal variations (Figure S4-8).  $\text{NO}_3^-$ ,  $\text{HNO}_3$ , and  $\text{NH}_4^+$  displayed the highest and  
288 lowest values in winter (December-February) and summer (June-August), respectively. On the one  
289 hand, the anthropogenic  $\text{NO}_x$  emission for domestic heating might be higher in winter compared  
290 with other seasons (Lin et al., 2011). On the other hand, the stagnant meteorological conditions  
291 limited the pollutant diffusion (Li et al., 2019b; Liu et al., 2020c). Meanwhile, the higher relative  
292 humidity in winter facilitated the formation of  $\text{NH}_4\text{NO}_3$  (Huang et al., 2016; Xu et al., 2012).  
293 However, both of ambient  $\text{NO}_3^-$  and  $\text{NH}_4^+$  concentrations showed the lower concentrations in  
294 summer, which might be attributable to the decomposition of  $\text{NH}_4\text{NO}_3$  under the condition of high  
295 air temperature. In contrast to the secondary inorganic nitrogen, the ambient  $\text{NH}_3$  level showed the  
296 highest concentration in summer ( $1.71 \pm 0.45 \mu\text{g N m}^{-3}$ ). China, Europe, and the United States  
297 suffered from similar  $\text{NH}_3$  peaks in summer ( $4.20 \pm 1.85$ ,  $1.77 \pm 0.65$ , and  $2.21 \pm 1.04 \mu\text{g N m}^{-3}$ ).  
298 There are two reasons accounting for the fact. At first, mineral N fertilizer or manure application  
299 was mainly performed in spring and early summer (Paulot et al., 2014). Many field observations  
300 have obtained similar  $\text{NH}_3$  peak in summer (He et al., 2021; Pan et al., 2018). Moreover, summer  
301 often showed the higher air temperature, which promotes the volatilization of ammonium and limits  
302 the gas-to-particle of gaseous  $\text{NH}_3$  (Liu et al., 2019).

### 303 3.4 The historical trends of reactive nitrogen components during 2000-2019

304 The long-term trends of ambient  $\text{NO}_3^-$  ( $\text{NO}_3\text{-N}$ ),  $\text{HNO}_3$ ,  $\text{NH}_3$ , and  $\text{NH}_4^+$  ( $\text{NH}_4\text{-N}$ ) concentrations  
305 are shown in Figure 6 and Figure S9-12. The  $\text{NO}_3^-$  concentration in China displayed rapid increase  
306 (9.7%/yr) during 2000-2007, and then it kept the moderate increase (4.2%/yr) during 2007-2013.  
307 However, the  $\text{NO}_3^-$  ( $\text{NO}_3\text{-N}$ ) concentration in China experienced the drastic decrease (-2.6%/yr)  
308 since 2013. The ambient  $\text{HNO}_3$  and  $\text{NH}_4^+$  ( $\text{NH}_4\text{-N}$ ) concentrations showed similar trends during this  
309 period. Due to the impact of Clean Air Action, the concentrations of gaseous precursors (e.g.,  $\text{SO}_2$   
310 and  $\text{NO}_x$ ) suffered from substantial decreases, which could be transformed into nitrate and  
311 ammonium via heterogeneous reactions (Huang et al., 2019). However, the decreasing rates of  $\text{NO}_3^-$   
312 were still much lower than those of gaseous precursors (Li et al., 2023). On the one hand, it might  
313 be associated with the increased  $\text{O}_3$  level and enhanced atmospheric oxidation capacity (AOC),  
314 which led to an increase in the photochemical reaction rate of the secondary components (Wang et

315 al., 2019). On the other hand, strong SO<sub>2</sub> emission control under the Clean Air Action allowed more  
316 gaseous NH<sub>3</sub> to form nitrate. The ambient NH<sub>3</sub> level remained relatively stable status during 2000-  
317 2013, while it experienced rapid increases after 2013. The result was in good agreement with Liu et  
318 al. (2019). In fact, the ambient NH<sub>3</sub> level in North China Plain still experienced dramatic increase  
319 (> 0.2 μg N m<sup>-3</sup>/yr) during 2000-2013 because enhanced agricultural activities. Zhang et al. (2017)  
320 have demonstrated that the livestock manure and fertilizer application generally accounted for 43%  
321 and 36% of the agricultural NH<sub>3</sub> emission, respectively. Since 2013, the NH<sub>3</sub> concentration in the  
322 entire China suffered from rapid increase, which might be associated with the drastic decrease of  
323 sulfate. It was well known that NH<sub>3</sub> could react with HNO<sub>3</sub> and gaseous H<sub>2</sub>SO<sub>4</sub> to generate ammonia  
324 sulfate and ammonia nitrate (Wang et al., 2022; Wang et al., 2019). Substantial decreases of acidic  
325 gases (e.g., SO<sub>2</sub>) lead to the reduction of NH<sub>3</sub> conversion to ammonia salts in the atmosphere (Chen  
326 et al., 2019), which result in excess NH<sub>3</sub> remaining in the gaseous phase. Different from China, the  
327 reactive N concentrations in some other Asia and Africa countries especially India (NO<sub>3</sub><sup>-</sup>, HNO<sub>3</sub>,  
328 NH<sub>3</sub>, and NH<sub>4</sub><sup>+</sup>: 54%, 46%, 11%, and 94%), South Korea (76%, 42%, 40%, and 9%), Indonesia  
329 (21%, 5%, 14%, and 41%), Democratic Congo (9%, 16%, 145%, 41%), and West Africa Coast (4%,  
330 11%, 37%, and 106%) still exhibited stable increases during 2000-2019. The results indicated that  
331 no strong reactive N emission control measures were implemented in these countries, which should  
332 be further exerted imperatively.

333 Compared with China, the long-term trends of reactive nitrogen components Europe and the  
334 United States were relatively stable. In the Europe, the concentrations of NO<sub>3</sub><sup>-</sup> (NO<sub>3</sub>-N), HNO<sub>3</sub>, and  
335 NH<sub>3</sub> exhibited increases during 2000-2007 (0.7%/yr, 2.3%/yr, and 2.1%/yr), while they experienced  
336 slight decreases after 2007. The NH<sub>4</sub><sup>+</sup> (NH<sub>4</sub>-N) level displayed continuous decrease since 2000. The  
337 result was closely linked with the trends of NO<sub>x</sub> and NH<sub>3</sub> emissions derived from satellite retrieval  
338 (Cooper et al., 2017; Luo et al., 2022). In the United States, both of NO<sub>3</sub><sup>-</sup> and NH<sub>4</sub><sup>+</sup> showed persistent  
339 decreases during 2000-2019. Zhang et al. (2018) have confirmed that NO<sub>x</sub> emission in the eastern  
340 US has experienced persistent decrease since 1990, which facilitated the decreases of NO<sub>3</sub><sup>-</sup> and  
341 NH<sub>4</sub><sup>+</sup> levels. However, the ambient HNO<sub>3</sub> and NH<sub>3</sub> concentrations displayed slight increases during  
342 2000-2007 (2.1%/yr), and then remained relatively stable since 2007. Liu et al. (2019) also found  
343 similar characteristic of ambient NH<sub>3</sub> trend in the United States. In fact, the NH<sub>3</sub> concentrations in

344 the Middle Plain and eastern US still showed increases due to the lack of NH<sub>3</sub> emission control  
345 policies as well as the decline in acidic gases (Warner et al., 2017). The reactive N concentrations  
346 in some countries in South America such as Brazil (9%, 0%, 13%, and 34%) and Argentina (10%,  
347 12%, 18%, and 7%) also remained relatively stable because local anthropogenic emission of reactive  
348 N did not show dramatic increases in the past two decades (McDuffie et al., 2020).

### 349 3.5 Projection of future ambient reactive nitrogen components

350 For the future reactive nitrogen component estimates, the ensemble model was applied to  
351 predict the reactive nitrogen component concentrations under the SSP1-2.6, SSP2-4.5, SSP3-7.0,  
352 and SSP5-8.5 scenarios. SSP1-2.6 represents the low emission pathways. In SSP1-2.6, the projected  
353 average NO<sub>3</sub><sup>-</sup> concentrations in most countries experienced rapid decreases from 2020 to 2100  
354 (Figure 7 and Table 1). The mean concentrations of NO<sub>3</sub><sup>-</sup> in China, India, Europe, and the United  
355 States decreased from  $1.16 \pm 0.35$ ,  $1.23 \pm 0.42$ ,  $0.41 \pm 0.14$ , and  $0.27 \pm 0.09$   $\mu\text{g N m}^{-3}$  to  $0.33 \pm 0.10$ ,  
356  $0.65 \pm 0.21$ ,  $0.10 \pm 0.03$ , and  $0.06 \pm 0.02$   $\mu\text{g N m}^{-3}$  during 2020-2100 in SSP1-2.6 scenario,  
357 respectively. Besides, the NO<sub>3</sub><sup>-</sup> concentrations in many other countries of Africa and South America  
358 such as Brazil (-127%) and Democratic Congo (-162%) also suffered from drastic decreases in this  
359 scenario. SSP2-4.5 scenario represents the middle range of plausible future pathways (Nazarenko  
360 et al., 2022). In this scenario, the predicted average NO<sub>3</sub><sup>-</sup> concentrations in China, India, Europe,  
361 and the United States decreased from  $1.19 \pm 0.40$ ,  $1.43 \pm 0.35$ ,  $0.44 \pm 0.13$ , and  $0.24 \pm 0.08$   $\mu\text{g N}$   
362  $\text{m}^{-3}$  to  $0.41 \pm 0.14$ ,  $0.95 \pm 0.32$ ,  $0.24 \pm 0.08$ , and  $0.05 \pm 0.02$   $\mu\text{g N m}^{-3}$  during 2020-2100, respectively.  
363 SSP3-7.0 and SSP5-8.5 denote the less investment in the environment and heavily relies on  
364 traditional energy for rapid economic development, respectively. The ambient NO<sub>3</sub><sup>-</sup> in these  
365 scenarios generally showed the higher concentrations compared with other scenarios. For instance,  
366 the NO<sub>3</sub><sup>-</sup> concentrations in China reduced from  $1.25 \pm 0.40$  (SSP3-7.0) and  $1.21 \pm 0.39$  (SSP5-8.5)  
367 to  $0.75 \pm 0.25$  (SSP3-7.0) and  $0.58 \pm 0.18$  (SSP5-8.5)  $\mu\text{g N m}^{-3}$  during 2020-2100 (Figure 8),  
368 respectively. The higher NO<sub>3</sub><sup>-</sup> concentrations in SSP3-7.0 and SSP5-8.5 might be associated with  
369 the higher anthropogenic NO<sub>x</sub> emission. Compared with SSP1-2.6 and SSP2-4.5, the NO<sub>3</sub><sup>-</sup>  
370 concentrations in some countries during SSP3-7.0 and SSP5-8.5 scenarios displayed slight increases  
371 from 2020 to 2040. For instance, the ambient NO<sub>3</sub><sup>-</sup> concentrations in Indonesia increased by 12%  
372 (SSP3-7.0) and 5% (SSP5-8.5), respectively.

373 The temporal variations of ambient HNO<sub>3</sub> were similar to those of NO<sub>3</sub><sup>-</sup> concentrations. The  
374 mean concentrations of HNO<sub>3</sub> in China, India, Europe, and the United States decreased from 0.25  
375 ± 0.09, 0.50 ± 0.16, 0.18 ± 0.06, and 0.08 ± 0.03 μg N m<sup>-3</sup> to 0.05 ± 0.01, 0.24 ± 0.08, 0.05 ± 0.02,  
376 and 0.03 ± 0.01 μg N m<sup>-3</sup> during 2020-2100 in SSP1-2.6 scenario (Figure S13-S14 and Table S3),  
377 respectively. However, the decreasing ratios of ambient HNO<sub>3</sub> levels especially in some developing  
378 countries such as Democratic Congo (-13%) and West Africa Coast (-47%) were much less than  
379 those of ambient NO<sub>3</sub><sup>-</sup> levels. For the SSP3-7.0 and SSP5-8.5 scenarios, the HNO<sub>3</sub> levels in some  
380 developing countries such as Democratic Congo (18%), West Africa Coast (16%), Indonesia (13%)  
381 even experienced moderate increases. It was assumed that the government gave less investment in  
382 environment improvement and the anthropogenic emission did not show marked decrease under the  
383 condition of SSP3-7.0 scenario (Chen et al., 2023; Chen et al., 2020).

384 As shown in Figure S15-S18 and Table S4-S5, the higher ambient NH<sub>3</sub> and NH<sub>4</sub><sup>+</sup>  
385 concentrations also focused on India and North China. In SSP1-2.6, the ambient NH<sub>3</sub> (NH<sub>4</sub><sup>+</sup>)  
386 concentrations in China, India, Europe, and the United States decreased from 3.51 ± 1.12 (2.00 ±  
387 0.62), 6.30 ± 2.12 (4.26 ± 1.42), 1.54 ± 0.51 (0.75 ± 0.24), and 1.79 ± 0.59 (0.53 ± 0.17) μg N m<sup>-3</sup>  
388 to 1.75 ± 0.58 (0.58 ± 0.19), 2.57 ± 0.85 (1.25 ± 0.41), 1.15 ± 0.36 (0.50 ± 0.16), and 1.58 ± 0.52  
389 (0.45 ± 0.15) μg N m<sup>-3</sup> during 2020-2100. Compared with SSP1-2.6, the ambient NH<sub>3</sub> and NH<sub>4</sub><sup>+</sup>  
390 concentrations in heavy-pollution scenarios (SSP3-7.0, and SSP5-8.5) scenarios did not show  
391 marked decreases from 2020-2100. Some developing countries such as Argentina (9%), Democratic  
392 Congo (25%), and West Africa Coast (24%) even suffered from persistent increases of ambient NH<sub>3</sub>  
393 and NH<sub>4</sub><sup>+</sup> levels. It might be associated with ineffective control of NH<sub>3</sub> emission compared with  
394 NO<sub>x</sub> emission.

### 395 3.6 Conclusions and limitations

396 The ground-level ambient reactive nitrogen observations, satellite retrievals, GEOS-Chem  
397 model output, and many other geographical covariates were integrated into the multi-stage model  
398 to reveal the global patterns of ambient reactive nitrogen components during 2000-2019. Then, these  
399 high-resolution reactive nitrogen dataset during the historical period was then utilized as the  
400 constraint to calibrate the CMIP6 dataset in four scenarios during 2020-2100. The results indicated  
401 the cross-validation (CV) R<sup>2</sup> values of four reactive nitrogen species showed satisfied performance

402 ( $R^2 > 0.55$ ). At the spatial scale, four reactive nitrogen components exhibited the higher  
403 concentrations in China and India. For the temporal variations, the concentrations of estimated  
404 ambient reactive nitrogen components in China experienced persistent increases during 2000-2013,  
405 while they suffered from drastic decreases since 2013 except  $\text{NH}_3$ , which might be linked with the  
406 impact of clean air policy. However, the concentrations of these species in Europe and the United  
407 States remained relatively stable since 2000. In the future scenarios, SSP3-7.0 (traditional energy  
408 scenario) and SSP1-2.6 (carbon neutrality scenario) displayed the highest and lowest reactive  
409 nitrogen component concentrations, respectively.

410 Global trends of four reactive nitrogen components during 2000-2100 emphasizes the urgent  
411 mitigation measures (carbon neutrality pathway) to reduce precursor emissions in order to decrease  
412 the concentrations and depositions of reactive nitrogen components especially in China and India.  
413 Furthermore, our result could give valuable insights into the impact of reactive nitrogen components  
414 on human health and ecological environment. However, this study still shows some limitations. First  
415 of all, the observation networks mainly focus on China, Europe, and the United States, and thus the  
416 simulations in many other regions might show large uncertainties. Secondly, both of the GEOS-  
417 Chem output and CMIP6 future climate scenario data also exhibits large uncertainties, which could  
418 impact the reliability of this study. Lastly, our predictions were performed on the basis of the premise  
419 that the world was steadily developing, and cannot predict the impacts of uncontrollable factors  
420 (e.g., COVID-19, Russia-Ukraine War).

#### 421 **Competing interests**

422 The contact author has declared that none of the authors has any competing interests.

#### 423 **Acknowledgements**

424 This work was supported by the National Natural Science Foundation of China (U23A2030),  
425 Shanghai Rehabilitation Medical Association health management research project (2023JGKT32),  
426 Academic Mentorship for Scientific Research Cadre Project (AMSCP-24-05-03).

#### 427 **Data availability**

428 The CMIP6 dataset used in this publication is available in <https://esgf.nci.org.au/projects/cmip6-nci/>.

#### 430 **Author contributions**

431 LR, SWW, and WGH designed the study; LR developed the model; GYN, ZLJ, XTZ, and SYB  
432 analyzed the observation and model data. LR wrote this manuscript.  
433



434 **References**

- 435 Altieri, K.E., Fawcett, S.E., Hastings, M.G. (2021) Reactive nitrogen cycling in the atmosphere and  
436 ocean. *Annual Review of Earth and Planetary Sciences* 49, 523-550.
- 437 Amante, C., Eakins, B.W. (2009) ETOPO1 arc-minute global relief model: procedures, data sources and  
438 analysis.
- 439 Bouwman, A., Van Vuuren, D., Derwent, R., Posch, M. (2002) A global analysis of acidification and  
440 eutrophication of terrestrial ecosystems. *Water, Air, and Soil Pollution* 141, 349-382.
- 441 Chen, H., Li, D., Gurnesa, G.A., Yu, G., Li, L., Zhang, W., Fang, H., Mo, J. (2015) Effects of nitrogen  
442 deposition on carbon cycle in terrestrial ecosystems of China: A meta-analysis. *Environmental  
443 pollution* 206, 352-360.
- 444 Chen, W., Lu, X., Yuan, D., Chen, Y., Li, Z., Huang, Y., Fung, T., Sun, H., Fung, J.C. (2023) Global PM2.  
445 5 Prediction and Associated Mortality to 2100 under Different Climate Change Scenarios.  
446 *Environmental science & technology* 57, 10039-10052.
- 447 Chen, X., Wang, Y.-h., Ye, C., Zhou, W., Cai, Z.-c., Yang, H., Han, X. (2018) Atmospheric nitrogen  
448 deposition associated with the eutrophication of Taihu Lake. *Journal of Chemistry* 2018.
- 449 Chen, Y., Liu, A., Cheng, X. (2020) Quantifying economic impacts of climate change under nine future  
450 emission scenarios within CMIP6. *Science of the Total Environment* 703, 134950.
- 451 Chen, Y., Shen, H., Russell, A.G. (2019) Current and future responses of aerosol pH and composition in  
452 the US to declining SO<sub>2</sub> emissions and increasing NH<sub>3</sub> emissions. *Environmental science &  
453 technology* 53, 9646-9655.
- 454 Chen, Y., Zhang, L., Henze, D.K., Zhao, Y., Lu, X., Winiwarter, W., Guo, Y., Liu, X., Wen, Z., Pan, Y.  
455 (2021) Interannual variation of reactive nitrogen emissions and their impacts on PM2.5 air pollution  
456 in China during 2005–2015. *Environmental Research Letters* 16, 125004.
- 457 Cooper, M., Martin, R.V., Padmanabhan, A., Henze, D.K. (2017) Comparing mass balance and adjoint  
458 methods for inverse modeling of nitrogen dioxide columns for global nitrogen oxide emissions.  
459 *Journal of Geophysical Research: Atmospheres* 122, 4718-4734.
- 460 Cooper, M.J., Martin, R.V., Hammer, M.S., Levelt, P.F., Veefkind, P., Lamsal, L.N., Krotkov, N.A., Brook,  
461 J.R., McLinden, C.A. (2022) Global fine-scale changes in ambient NO<sub>2</sub> during COVID-19 lockdowns.  
462 *Nature* 601, 380-387.
- 463 Cui, L. (2023) Impact of COVID-19 restrictions on the concentration and source apportionment of  
464 atmospheric ammonia (NH<sub>3</sub>) across India. *Science of the Total Environment* 881, 163443.
- 465 Drury, E., Jacob, D.J., Spurr, R.J.D., Wang, J., Shinozuka, Y., Anderson, B.E., Clarke, A.D., Dibb, J.,  
466 McNaughton, C. Weber, D., Synthesis of satellite (MODIS), aircraft (ICARTT), and surface  
467 (IMPROVE, EPA-AQS, AERONET) aerosol observations over eastern North America to improve  
468 MODIS aerosol retrievals and constrain surface aerosol concentrations and sources *J. Geophys. Res.  
469 Atmos.*, 115 (2010), p. D14204.
- 470 Du, E., de Vries, W., Galloway, J.N., Hu, X., Fang, J. (2014) Changes in wet nitrogen deposition in the  
471 United States between 1985 and 2012. *Environmental Research Letters* 9, 095004.
- 472 Ehrnsperger, L., Klemm, O. (2021) Source apportionment of urban ammonia and its contribution to  
473 secondary particle formation in a Mid-size European City. *Aerosol and Air Quality Research* 21,  
474 200404.
- 475 Feng, X., Lin, H., Fu, T.-M., Sulprizio, M.P., Zhuang, J., Jacob, D.J., Tian, H., Ma, Y., Zhang, L., Wang,  
476 X. (2021) WRF-GC (v2. 0): online two-way coupling of WRF (v3. 9.1. 1) and GEOS-Chem (v12. 7.2)  
477 for modeling regional atmospheric chemistry–meteorology interactions. *Geoscientific Model*

478 Development 14, 3741-3768.

479 Geddes, J.A., Martin, R.V. (2017) Global deposition of total reactive nitrogen oxides from 1996 to 2014  
480 constrained with satellite observations of NO<sub>2</sub> columns. *Atmos. Chem. Phys.* 17, 10071-10091.

481 He, Y., Pan, Y., Gu, M., Sun, Q., Zhang, Q., Zhang, R., Wang, Y. (2021) Changes of ammonia  
482 concentrations in wintertime on the North China Plain from 2018 to 2020. *Atmospheric Research* 253,  
483 105490.

484 He, Z., Liu, P., Zhao, X., He, X., Liu, J., Mu, Y. (2022) Responses of surface O<sub>3</sub> and PM<sub>2.5</sub> trends to  
485 changes of anthropogenic emissions in summer over Beijing during 2014–2019: A study based on  
486 multiple linear regression and WRF-Chem. *Science of the Total Environment* 807, 150792.

487 Hoesly, R.M., Smith, S.J., Feng, L., Klimont, Z., Janssens-Maenhout, G., Pitkanen, T., Seibert, J.J., Vu,  
488 L., Andres, R.J., Bolt, R.M. (2018) Historical (1750–2014) anthropogenic emissions of reactive gases  
489 and aerosols from the Community Emissions Data System (CEDS). *Geoscientific Model Development*  
490 11, 369-408.

491 Huang, L., An, J., Koo, B., Yarwood, G., Yan, R., Wang, Y., Huang, C., Li, L. (2019) Sulfate formation  
492 during heavy winter haze events and the potential contribution from heterogeneous SO<sub>2</sub> + NO<sub>2</sub>  
493 reactions in the Yangtze River Delta region, China. *Atmospheric Chemistry and Physics* 19, 14311-  
494 14328.

495 Huang, T., Chen, J., Zhao, W., Cheng, J., Cheng, S. (2016) Seasonal variations and correlation analysis  
496 of water-soluble inorganic ions in PM<sub>2.5</sub> in Wuhan, 2013. *Atmosphere* 7, 49.

497 Huang, X., Liu, Z., Liu, J., Hu, B., Wen, T., Tang, G., Zhang, J., Wu, F., Ji, D., Wang, L. (2017) Chemical  
498 characterization and source identification of PM<sub>2.5</sub> at multiple sites in the Beijing–Tianjin–Hebei  
499 region, China. *Atmospheric Chemistry and Physics* 17, 12941-12962.

500 Huneus, N., Granier, C., Dawidowski, L., van Der Gon, H.D., Alonso, M., Castesana, P., Diaz, M., Frost,  
501 G.J., Gallardo, L., Gomez, D., (2017) Anthropogenic emissions in South America for air quality and  
502 climate modelling, 2017 International Emission Inventory Conference “Applying Science and  
503 Streamlining Processes to Improve Inventories”.

504 Kang, Y., Liu, M., Song, Y., Huang, X., Yao, H., Cai, X., Zhang, H., Kang, L., Liu, X., Yan, X. (2016)  
505 High-resolution ammonia emissions inventories in China from 1980 to 2012. *Atmospheric Chemistry*  
506 *and Physics* 16, 2043-2058.

507 Karra, K., Kontgis, C., Statman-Weil, Z., Mazzariello, J.C., Mathis, M., Brumby, S.P., (2021) Global  
508 land use/land cover with Sentinel 2 and deep learning, 2021 IEEE international geoscience and remote  
509 sensing symposium IGARSS. IEEE, pp. 4704-4707.

510 Kim, H.C., Lee, P., Judd, L., Pan, L., Lefer, B. (2016) OMI NO<sub>2</sub> column densities over North American  
511 urban cities: the effect of satellite footprint resolution. *Geoscientific Model Development* 9, 1111-1123.

512 Li, H., Yang, Y., Wang, H., Wang, P., Yue, X., Liao, H. (2022) Projected aerosol changes driven by  
513 emissions and climate change using a machine learning method. *Environmental science & technology*  
514 56, 3884-3893.

515 Li, H., Zhang, Q., Zhang, Q., Chen, C., Wang, L., Wei, Z., Zhou, S., Parworth, C., Zheng, B., Canonaco,  
516 F. (2017) Wintertime aerosol chemistry and haze evolution in an extremely polluted city of the North  
517 China Plain: significant contribution from coal and biomass combustion. *Atmospheric Chemistry and*  
518 *Physics* 17, 4751-4768. Li, M.; Kurokawa, J.; Zhang, Q.; Woo, J.-H.; Morikawa, T.; Chatani, S.; Lu,  
519 Z.; Song, Y.; Geng, G.; Hu, H., MIXv2: a long-term mosaic emission inventory for Asia (2010-2017).  
520 *Atmospheric Chemistry and Physics* 2024, 24, (7), 3925-3952.

521 Li, R., Cui, L., Fu, H., Zhao, Y., Zhou, W., Chen, J. (2020) Satellite-Based Estimates of Wet Ammonium

522 (NH<sub>4</sub>-N) Deposition Fluxes Across China during 2011–2016 Using a Space–Time Ensemble Model.  
523 Environmental science & technology 54, 13419-13428.

524 Li, R., Cui, L., Zhao, Y., Zhang, Z., Sun, T., Li, J., Zhou, W., Meng, Y., Huang, K., Fu, H. (2019a) Wet  
525 deposition of inorganic ions in 320 cities across China: spatio-temporal variation, source  
526 apportionment, and dominant factors. Atmospheric Chemistry and Physics 19, 11043-11070.

527 Li, R., Gao, Y., Xu, J., Cui, L., Wang, G. (2023) Impact of Clean Air Policy on Criteria Air Pollutants  
528 and Health Risks Across China During 2013-2021. Journal of Geophysical Research: Atmospheres  
529 128, e2023JD038939.

530 Li, R., Wang, Z., Cui, L., Fu, H., Zhang, L., Kong, L., Chen, W., Chen, J. (2019b) Air pollution  
531 characteristics in China during 2015-2016: Spatiotemporal variations and key meteorological factors.  
532 Science of the Total Environment 648, 902-915.

533 Li, Y., Schichtel, B.A., Walker, J.T., Schwede, D.B., Chen, X., Lehmann, C.M., Puchalski, M.A., Gay,  
534 D.A., Collett Jr, J.L. (2016) Increasing importance of deposition of reduced nitrogen in the United  
535 States. Proceedings of the National Academy of Sciences 113, 5874-5879.

536 Lin, J.T., McElroy, M.B., (2010) Impacts of boundary layer mixing on pollutant vertical profiles in the  
537 lower troposphere: implications to satellite remote sensing Atmos. Environ., 44, pp. 1726-1739.

538 Lin, W., Xu, X., Ge, B., Liu, X. (2011) Gaseous pollutants in Beijing urban area during the heating period  
539 2007-2008: variability, sources, meteorological, and chemical impacts. Atmospheric Chemistry and  
540 Physics 11, 8157-8170.

541 Liu, H., Gong, P., Wang, J., Clinton, N., Bai, Y., Liang, S. (2020a) Annual dynamics of global land cover  
542 and its long-term changes from 1982 to 2015. Earth System Science Data 12, 1217-1243.

543 Liu, H., Jacob, D.J., Bey, I., Yantosca, R.M. (2001) Constraints from 210Pb and 7Be on wet deposition  
544 and transport in a global three-dimensional chemical tracer model driven by assimilated  
545 meteorological fields. Journal of Geophysical Research: Atmospheres 106, 12109-12128.

546 Liu, L., Yang, Y., Xi, R., Zhang, X., Xu, W., Liu, X., Li, Y., Liu, P., Wang, Z. (2021) Global Wet-Reduced  
547 Nitrogen Deposition Derived From Combining Satellite Measurements With Output From a Chemistry  
548 Transport Model. Journal of Geophysical Research: Atmospheres 126, e2020JD033977.

549 Liu, L., Zhang, X., Wong, A.Y., Xu, W., Liu, X., Li, Y., Mi, H., Lu, X., Zhao, L., Wang, Z. (2019)  
550 Estimating global surface ammonia concentrations inferred from satellite retrievals. Atmospheric  
551 Chemistry and Physics 19, 12051-12066.

552 Liu, L., Zhang, X., Xu, W., Liu, X., Lu, X., Wei, J., Li, Y., Yang, Y., Wang, Z., Wong, A.Y. (2020b)  
553 Reviewing global estimates of surface reactive nitrogen concentration and deposition using satellite  
554 retrievals. Atmospheric Chemistry and Physics 20, 8641-8658.

555 Liu, Y., Zhou, Y., Lu, J. (2020c) Exploring the relationship between air pollution and meteorological  
556 conditions in China under environmental governance. Scientific reports 10, 14518.

557 Luo, Z., Zhang, Y., Chen, W., Van Damme, M., Coheur, P.-F., Clarisse, L. (2022) Estimating global  
558 ammonia (NH<sub>3</sub>) emissions based on IASI observations from 2008 to 2018. Atmospheric Chemistry  
559 and Physics 22, 10375-10388.

560 Ma, R., Yu, K., Xiao, S., Liu, S., Ciais, P., Zou, J. (2022) Data-driven estimates of fertilizer-induced soil  
561 NH<sub>3</sub>, NO and N<sub>2</sub>O emissions from croplands in China and their climate change impacts. Global  
562 Change Biology 28, 1008-1022.

563 McDuffie, E.E., Smith, S.J., O'Rourke, P., Tibrewal, K., Venkataraman, C., Marais, E.A., Zheng, B.,  
564 Crippa, M., Brauer, M., Martin, R.V. (2020) A global anthropogenic emission inventory of atmospheric  
565 pollutants from sector-and fuel-specific sources (1970–2017): an application of the Community

566 Emissions Data System (CEDs). *Earth System Science Data* 12, 3413-3442.

567 Nazarenko, L.S., Tausnev, N., Russell, G.L., Rind, D., Miller, R.L., Schmidt, G.A., Bauer, S.E., Kelley,  
568 M., Ruedy, R., Ackerman, A.S. (2022) Future climate change under SSP emission scenarios with  
569 GISS-E2. 1. *Journal of Advances in Modeling Earth Systems* 14, e2021MS002871.

570 Pan, Y., Tian, S., Zhao, Y., Zhang, L., Zhu, X., Gao, J., Huang, W., Zhou, Y., Song, Y., Zhang, Q. (2018)  
571 Identifying ammonia hotspots in China using a national observation network. *Environmental science  
572 & technology* 52, 3926-3934.

573 Paulot, F., Jacob, D.J., Pinder, R., Bash, J., Travis, K., Henze, D. (2014) Ammonia emissions in the  
574 United States, European Union, and China derived by high-resolution inversion of ammonium wet  
575 deposition data: Interpretation with a new agricultural emissions inventory (MASAGE\_NH3). *Journal  
576 of Geophysical Research: Atmospheres* 119, 4343-4364.

577 Potapov, P., Hansen, M.C., Pickens, A., Hernandez-Serna, A., Tyukavina, A., Turubanova, S., Zalles, V.,  
578 Li, X., Khan, A., Stolle, F. (2022) The global 2000-2020 land cover and land use change dataset  
579 derived from the Landsat archive: first results. *Frontiers in Remote Sensing* 3, 856903.

580 Qi, L., Zheng, H., Ding, D., Wang, S. (2023) Responses of sulfate and nitrate to anthropogenic emission  
581 changes in eastern China-in perspective of long-term variations. *Science of the Total Environment* 855,  
582 158875.

583 Qu, Z., Henze, D.K., Cooper, O.R., Neu, J.L. (2020) Impacts of global NO<sub>x</sub> inversions on NO<sub>2</sub> and  
584 ozone simulations. *Atmospheric Chemistry and Physics* 20, 13109-13130.

585 Shi, X., Zhao, C., Jiang, J.H., Wang, C., Yang, X., Yung, Y.L. (2018) Spatial representativeness of PM<sub>2.5</sub>  
586 concentrations obtained using observations from network stations. *Journal of Geophysical Research:  
587 Atmospheres* 123, 3145-3158.

588 Van Damme, M., Whitburn, S., Clarisse, L., Clerbaux, C., Hurtmans, D., Coheur, P.-F. (2017) Version 2  
589 of the IASI NH<sub>3</sub> neural network retrieval algorithm: near-real-time and reanalysed datasets.  
590 *Atmospheric Measurement Techniques* 10, 4905-4914.

591 Von Schneidemesser, E., Monks, P.S., Allan, J.D., Bruhwiler, L., Forster, P., Fowler, D., Lauer, A.,  
592 Morgan, W.T., Paasonen, P., Righi, M. (2015) Chemistry and the linkages between air quality and  
593 climate change. *Chemical reviews* 115, 3856-3897.

594 Wang, M., Xiao, M., Bertozzi, B., Marie, G., Rörup, B., Schulze, B., Bardakov, R., He, X.-C., Shen, J.,  
595 Scholz, W. (2022) Synergistic HNO<sub>3</sub>-H<sub>2</sub>SO<sub>4</sub>-NH<sub>3</sub> upper tropospheric particle formation. *Nature* 605,  
596 483-489.

597 Wang, T., Song, Y., Xu, Z., Liu, M., Xu, T., Liao, W., Yin, L., Cai, X., Kang, L., Zhang, H., Zhu, T. (2020)  
598 Why is the Indo-Gangetic Plain the region with the largest NH<sub>3</sub> column in the globe during pre-  
599 monsoon and monsoon seasons? *Atmos. Chem. Phys.* 20, 8727-8736.

600 Wang, Y., Li, W., Gao, W., Liu, Z., Tian, S., Shen, R., Ji, D., Wang, S., Wang, L., Tang, G. (2019) Trends  
601 in particulate matter and its chemical compositions in China from 2013–2017. *Science China Earth  
602 Sciences* 62, 1857-1871.

603 Warner, J., Dickerson, R., Wei, Z., Strow, L.L., Wang, Y., Liang, Q. (2017) Increased atmospheric  
604 ammonia over the world's major agricultural areas detected from space. *Geophysical Research Letters*  
605 44, 2875-2884.

606 Wen, L., Xue, L., Wang, X., Xu, C., Chen, T., Yang, L., Wang, T., Zhang, Q., Wang, W. (2018)  
607 Summertime fine particulate nitrate pollution in the North China Plain: increasing trends, formation  
608 mechanisms and implications for control policy. *Atmospheric Chemistry and Physics* 18, 11261-11275.

609 Wesely, M. (2007) Parameterization of surface resistances to gaseous dry deposition in regional-scale

610 numerical models. *Atmospheric Environment* 41, 52-63.

611 Whitburn, S., Van Damme, M., Clarisse, L., Bauduin, S., Heald, C., Hadji-Lazaro, J., Hurtmans, D.,  
612 Zondlo, M.A., Clerbaux, C., Coheur, P.F. (2016a) A flexible and robust neural network IASI-NH<sub>3</sub>  
613 retrieval algorithm. *Journal of Geophysical Research: Atmospheres* 121, 6581-6599.

614 Whitburn, S., Van Damme, M., Clarisse, L., Turquety, S., Clerbaux, C., Coheur, P.F. (2016b) Doubling  
615 of annual ammonia emissions from the peat fires in Indonesia during the 2015 El Niño. *Geophysical*  
616 *Research Letters* 43, 11,007-011,014.

617 Xu, L., Chen, X., Chen, J., Zhang, F., He, C., Zhao, J., Yin, L. (2012) Seasonal variations and chemical  
618 compositions of PM<sub>2.5</sub> aerosol in the urban area of Fuzhou, China. *Atmospheric Research* 104, 264-  
619 272.

620 Xu, W., Zhang, L., Liu, X. (2019) A database of atmospheric nitrogen concentration and deposition from  
621 the nationwide monitoring network in China. *Scientific data* 6, 1-6.

622 Zaehle, S. (2013) Terrestrial nitrogen-carbon cycle interactions at the global scale. *Philosophical*  
623 *Transactions of the Royal Society B: Biological Sciences* 368, 20130125.

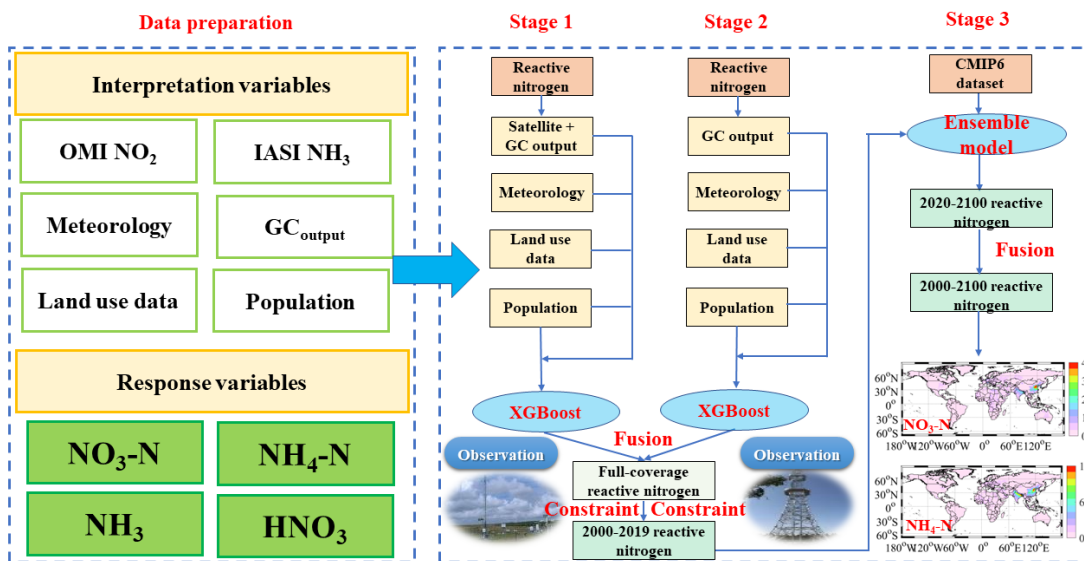
624 Zhang, L., Guo, X., Zhao, T., Gong, S., Xu, X., Li, Y., Luo, L., Gui, K., Wang, H., Zheng, Y. (2019) A  
625 modelling study of the terrain effects on haze pollution in the Sichuan Basin. *Atmospheric*  
626 *Environment* 196, 77-85.

627 Zhang, X., Ward, B.B., Sigman, D.M. (2020) Global nitrogen cycle: critical enzymes, organisms, and  
628 processes for nitrogen budgets and dynamics. *Chemical reviews* 120, 5308-5351.

629 Zhang, X., Wu, Y., Liu, X., Reis, S., Jin, J., Dragosits, U., Van Damme, M., Clarisse, L., Whitburn, S.,  
630 Coheur, P.-F. (2017) Ammonia emissions may be substantially underestimated in China.  
631 *Environmental science & technology* 51, 12089-12096.

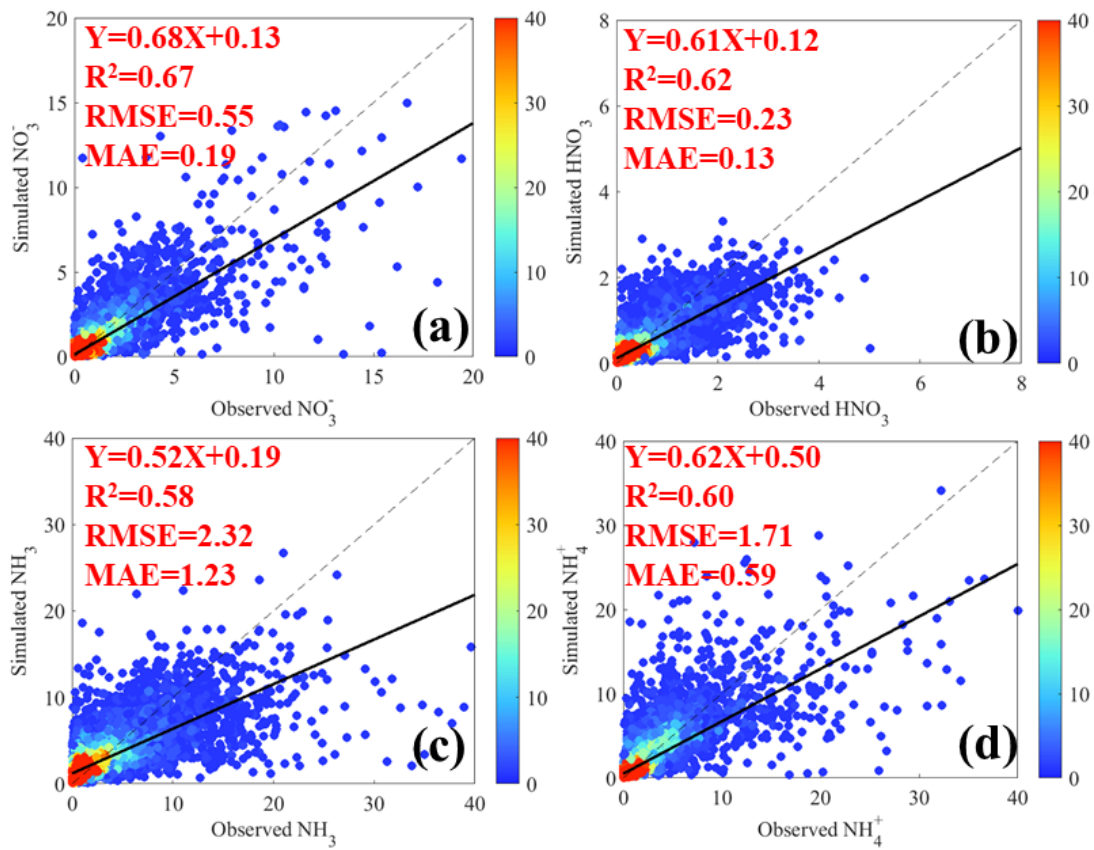
632 Zhang, Y., Mathur, R., Bash, J.O., Hogrefe, C., Xing, J., Roselle, S.J. (2018) Long-term trends in total  
633 inorganic nitrogen and sulfur deposition in the US from 1990 to 2010. *Atmospheric Chemistry and*  
634 *Physics* 18, 9091-9106.

635 **Figure 1** The workflow of global full-coverage reactive nitrogen estimates during 2000-2100.  
 636 GC<sub>output</sub> denotes the GEOS-Chem output.



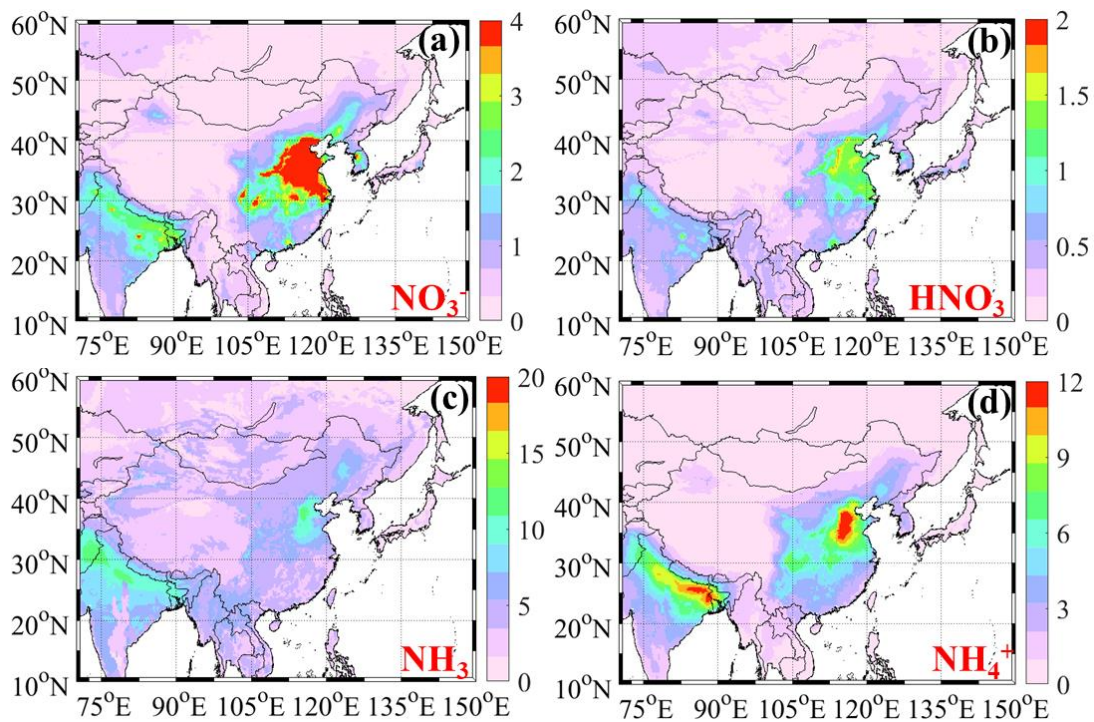
637

638 **Figure 2** The predictive performances of four reactive nitrogen components including  $\text{NO}_3^-$  ( $\text{NO}_3^-$ -  
 639 N) (a),  $\text{HNO}_3$  (b),  $\text{NH}_3$  (c), and  $\text{NH}_4^+$  ( $\text{NH}_4\text{-N}$ ) (d). The model was constructed with 90% original  
 640 data and the remained data was applied to validate the model. The black solid line denotes the best-  
 641 fitting curve for all of the points, while the black dashed line represents the diagonal, which means  
 642 the same observed and simulated values. The color scale denotes the sample size.



643

644 **Figure 3** The spatiotemporal variations of  $\text{NO}_3^-$  ( $\text{NO}_3\text{-N}$ ),  $\text{HNO}_3$ ,  $\text{NH}_3$ , and  $\text{NH}_4^+$  ( $\text{NH}_4\text{-N}$ )  
645 concentrations in East Asia (a-d) (Unit:  $\mu\text{g N m}^{-3}$ ).

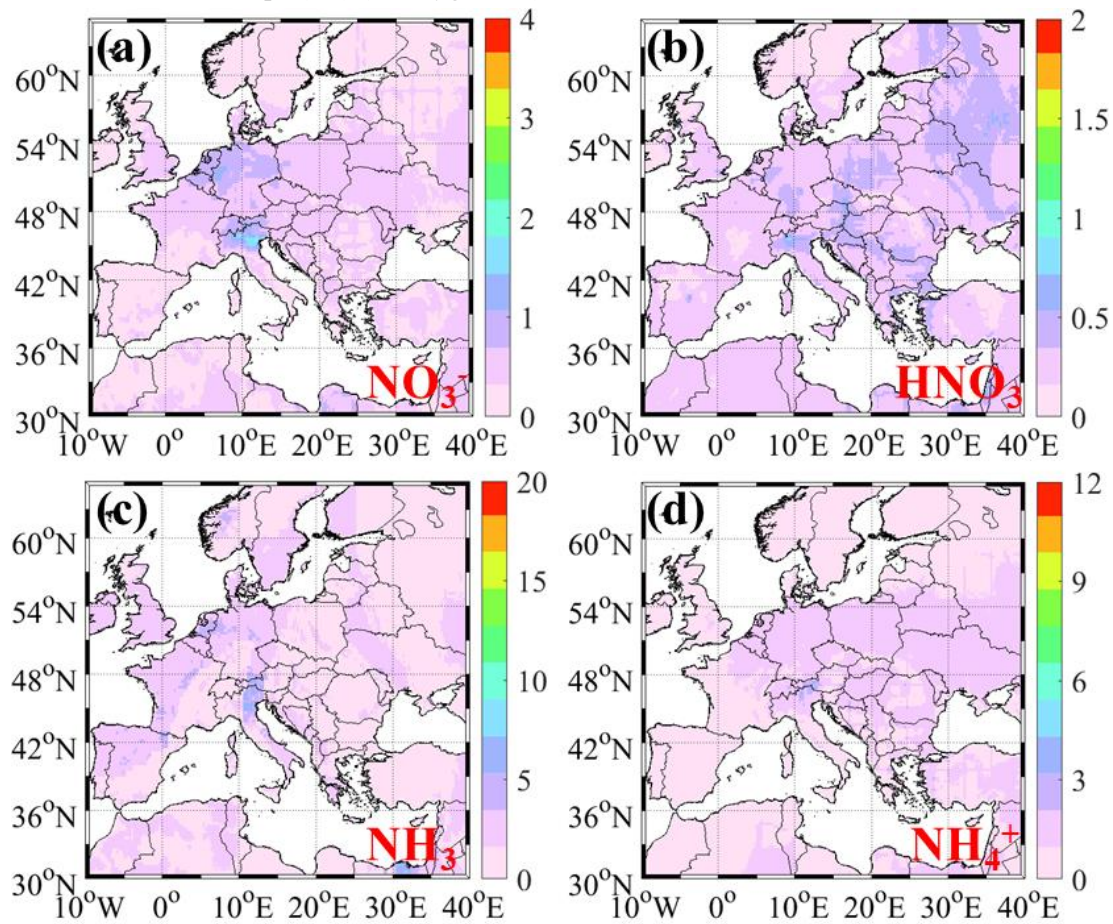


646

647

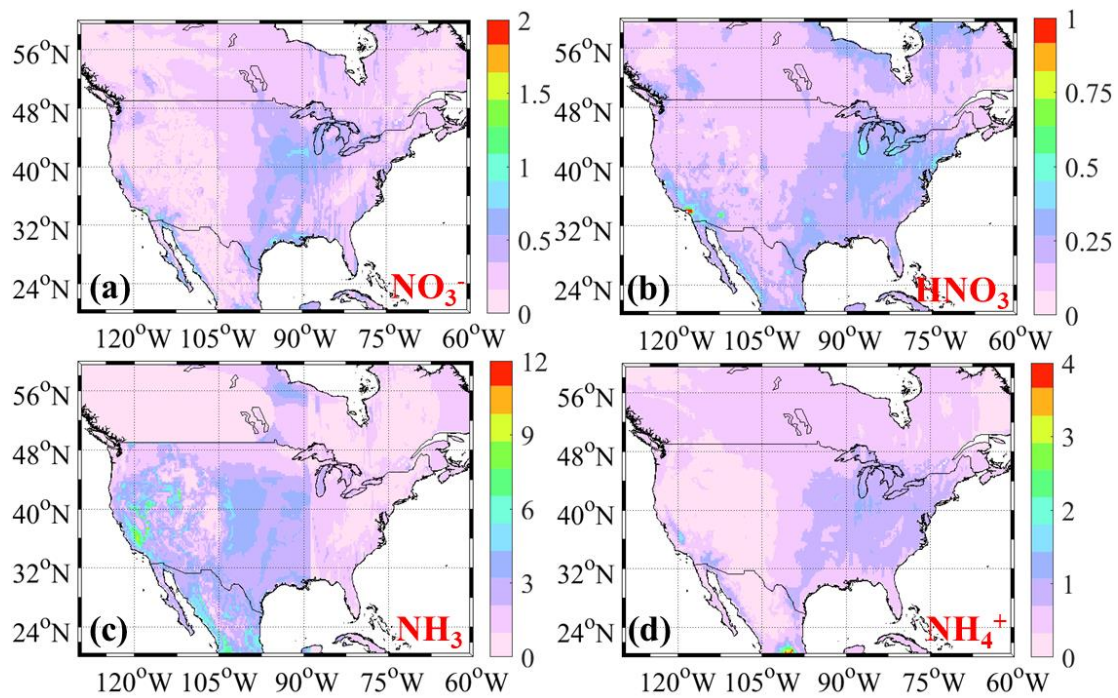


648 **Figure 4** The spatiotemporal variations of  $\text{NO}_3^-$  ( $\text{NO}_3\text{-N}$ ),  $\text{HNO}_3$ ,  $\text{NH}_3$ , and  $\text{NH}_4^+$  ( $\text{NH}_4\text{-N}$ )  
649 concentrations in Europe (a-d) (Unit:  $\mu\text{g N m}^{-3}$ ).



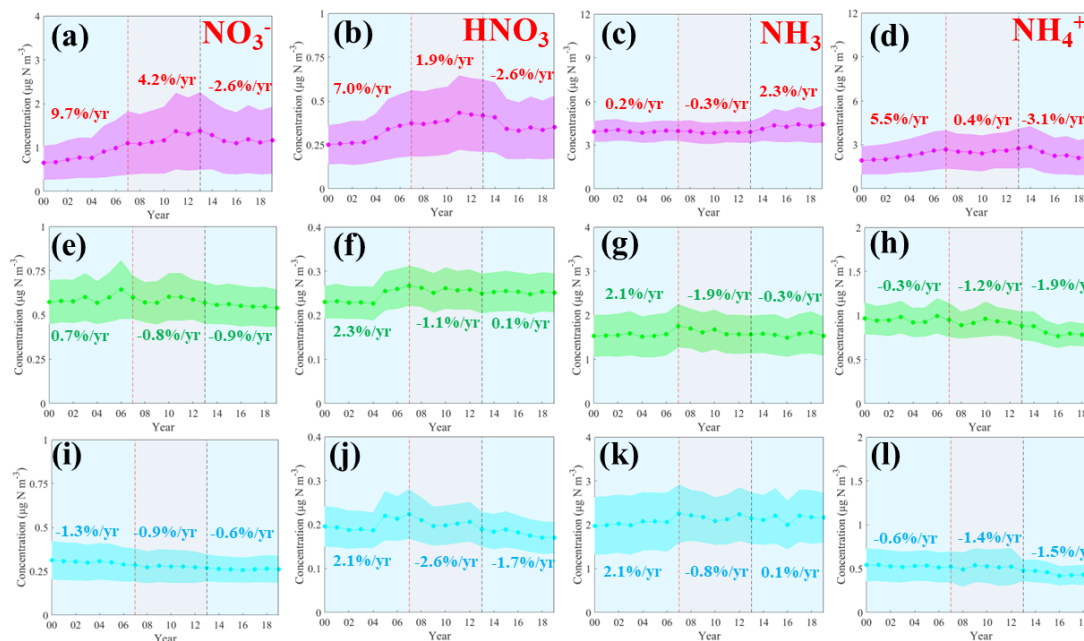
650  
651

652 **Figure 5** The spatiotemporal variations of  $\text{NO}_3^-$  ( $\text{NO}_3\text{-N}$ ),  $\text{HNO}_3$ ,  $\text{NH}_3$ , and  $\text{NH}_4^+$  ( $\text{NH}_4\text{-N}$ )  
653 concentrations in North America (a-d) (Unit:  $\mu\text{g N m}^{-3}$ ).



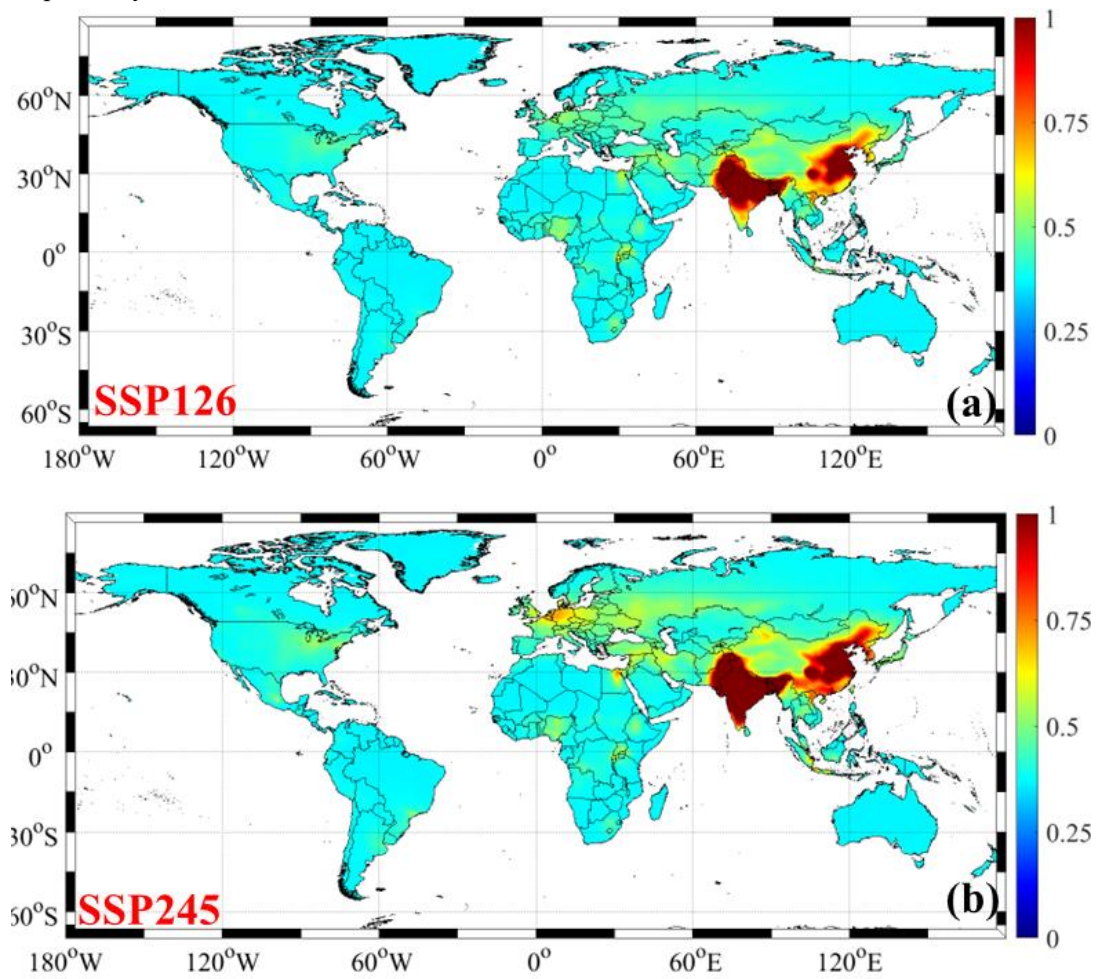
654

655 **Figure 6** The long-term variations of  $\text{NO}_3^-$  ( $\text{NO}_3\text{-N}$ ),  $\text{HNO}_3$ ,  $\text{NH}_3$ , and  $\text{NH}_4^+$  ( $\text{NH}_4\text{-N}$ ) concentrations  
 656 in China (pink), Europe (green), and the United States (cyan) (Unit:  $\mu\text{g N m}^{-3}$ ).



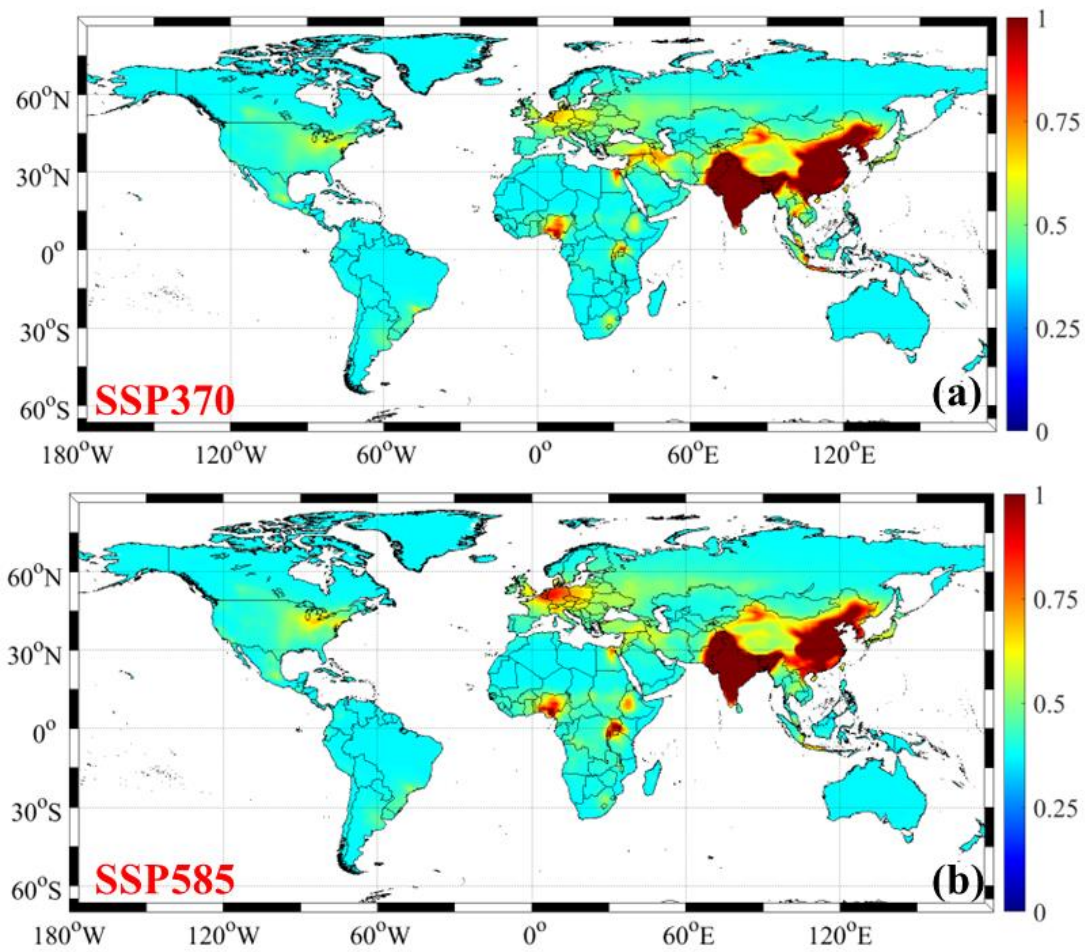
657

658 **Figure 7** Spatial variations of projected global ambient concentrations of reactive nitrogen  
659 components under different climate change scenarios (Unit:  $\mu\text{g N m}^{-3}$ ). Panels (a-b) represent the  
660 annual mean concentrations of ambient  $\text{NO}_3^-$  ( $\text{NO}_3\text{-N}$ ) under SSP1-2.6, SSP2-4.5 during 2021-2100,  
661 respectively.



662  
663

664 **Figure 8** Spatial variations of projected global ambient concentrations of reactive nitrogen  
665 components under different climate change scenarios (Unit:  $\mu\text{g N m}^{-3}$ ). Panels (a-b) represent the  
666 annual mean concentrations of ambient  $\text{NO}_3^-$  ( $\text{NO}_3\text{-N}$ ) under SSP3-7.0, and SSP5-8.5 during 2021-  
667 2100, respectively.



668  
669

670  
671

**Table 1** The temporal variations of ambient NO<sub>3</sub><sup>-</sup> (NO<sub>3</sub>-N) concentrations (average concentrations, Unit: µg N m<sup>-3</sup>) in selected countries during 2000-2100.

Scenario	NO <sub>3</sub> <sup>-</sup>	China	India	Europe	United States	Brazil	Argentina	Democratic Congo	West Africa Coast	Indonesia	South Korea
Historical	2000	0.66	0.95	0.57	0.31	0.29	0.21	0.56	0.30	0.31	1.06
	2005	0.91	1.26	0.60	0.30	0.31	0.22	0.56	0.30	0.34	1.38
	2010	1.17	1.53	0.60	0.28	0.33	0.23	0.58	0.31	0.32	1.43
	2013	1.39	1.63	0.57	0.27	0.30	0.24	0.58	0.31	0.33	1.57
	2015	1.16	1.34	0.56	0.26	0.32	0.22	0.58	0.32	0.45	1.88
	2019	1.18	1.46	0.54	0.26	0.32	0.23	0.61	0.32	0.37	1.87
SSP1-2.6	2020	1.16	1.23	0.41	0.27	0.25	0.18	0.55	0.28	0.34	1.81
	2040	0.82	1.12	0.28	0.10	0.21	0.14	0.62	0.32	0.28	1.46
	2060	0.69	1.01	0.15	0.05	0.18	0.13	0.43	0.25	0.24	0.69
	2080	0.41	0.89	0.12	0.05	0.17	0.12	0.32	0.17	0.20	0.39
	2100	0.33	0.65	0.10	0.06	0.11	0.08	0.21	0.11	0.16	0.23
SSP2-4.5	2020	1.19	1.43	0.44	0.24	0.26	0.19	0.52	0.29	0.37	1.85
	2040	1.09	1.35	0.43	0.16	0.22	0.16	0.57	0.31	0.35	1.80
	2060	0.89	1.22	0.35	0.11	0.20	0.15	0.51	0.27	0.32	1.25
	2080	0.63	1.06	0.29	0.07	0.17	0.12	0.42	0.23	0.23	0.68
	2100	0.41	0.95	0.24	0.05	0.14	0.10	0.36	0.19	0.20	0.38
SSP3-7.0	2020	1.25	1.59	0.53	0.33	0.31	0.22	0.64	0.34	0.42	1.95
	2040	1.36	1.50	0.47	0.24	0.26	0.19	0.61	0.33	0.47	1.89
	2060	1.18	1.35	0.42	0.19	0.22	0.16	0.56	0.30	0.41	1.56
	2080	0.96	1.15	0.36	0.16	0.18	0.13	0.54	0.29	0.35	1.35
	2100	0.75	1.08	0.33	0.12	0.15	0.11	0.51	0.27	0.30	1.24
SSP5-8.5	2020	1.21	1.50	0.53	0.28	0.28	0.20	0.57	0.31	0.37	1.91
	2040	1.28	1.42	0.49	0.23	0.25	0.18	0.60	0.32	0.39	1.85
	2060	1.05	1.30	0.47	0.24	0.20	0.15	0.55	0.29	0.35	1.44
	2080	0.86	1.10	0.44	0.25	0.15	0.11	0.50	0.27	0.29	1.26
	2100	0.58	1.02	0.31	0.20	0.13	0.09	0.46	0.25	0.25	1.05

672

673  
674